

## Electronic Supplementary Information of Phase diagram of binary colloidal rod-sphere mixtures from a 3D real-space analysis of sedimentation-diffusion equilibria<sup>†</sup>

Henriëtte E. Bakker,<sup>\*a</sup> Simone Dussi,<sup>a</sup> Barbera L. Droste,<sup>a</sup> Thijs H. Besseling,<sup>a</sup> Chris L. Kennedy,<sup>a</sup> Evert I. Wiegant,<sup>a</sup> Bing Liu,<sup>a,b</sup> Arnout Imhof,<sup>a</sup> Marjolein Dijkstra,<sup>a</sup> Alfons van Blaaderen,<sup>\*\*a</sup>

### SI 1 Determining effective particle dimensions

In order to compare experimental data with simulations, we determine first the effective dimensions of the particles that account for the thin electric double layer. The colloidal particles used act as nearly hard particles, with a dimension slightly larger than that derived from TEM images. First, to determine the effective diameter of the spheres,  $\sigma_{eff} = \sigma_{tem} + \lambda_s$ , we mapped the equation of state as obtained by integrating the density profile of the top part of the sediment (that contained only spheres) to the Carnahan-Starling (CS) equation of state (see Supplementary Fig. S7a).

$$\beta P / \rho_{sph} = \frac{1 + \phi + \phi^2 - \phi^3}{(1 - \phi)^3},$$

where  $\rho_{sph}$  is the number density of the spheres,  $\beta = 1/k_B T$ , and  $\phi = \rho v_{sph}$ , with  $v_{sph} = \frac{1}{6} \pi \sigma_{eff}^3$  the effective volume of one spherical particle. The pressure at height  $z$  in the sample was calculated using  $P(z) = m_{sph} g \int_z^h \rho_{sph}(z) dz$ , with  $m_{sph}$  the buoyant mass of the particles (calculated from TEM dimensions),  $g$  the gravitational acceleration constant,  $z$  the height in the sediment and  $h$  height of the sampled volume, where we made sure that the particle density vanished at  $h$ . The best fit with the CS equation of state was obtained by taking  $\lambda_s = 80$  nm for the volume fractions  $\phi < 0.2$  or pressures  $\beta P / \rho_{sph} < 2.5$ . The equation of state as obtained from experiments becomes unphysical at higher pressures (i.e., lower height  $z$  in the sediment) as the density of rods cannot be neglected at lower  $z$ . Next, in order to determine the effective dimensions of the rods,  $D_{eff} = D_{tem} + \lambda_r$  and  $L_{eff} = L_{tem} + \lambda_r$ , we mapped the jump in the global nematic order parameter  $S$  at the isotropic nematic transition of an equilibrated sample containing pure hard rods to results obtained from  $NPT$  simulations of only rods (see Supplementary Fig. S7b and discussion below). Experimental data with  $\lambda_r = 120$  nm matched best with data obtained from simulations. This resulted in the following effective dimensions for the R2 rods:  $D_{eff} = 707$  nm,  $L_{eff} = 3711$  nm,  $(L/D)_{eff} = 5.25$ ,  $D_{eff} = 1.52 \sigma_{eff}$ . We did not use the equation of state of rods to determine the effective dimensions of the rods as the equation of state is more sensitive to polydispersity.

For both procedures to find the effective dimensions, one should realize that discrepancies can arise due to polydispersity, which also can cause size segregation of particles with height.

### SI 2 Order parameters for colloidal rods

To distinguish between the isotropic and the different liquid crystalline phases we rely on global and local order parameters. The global nematic order parameter is obtained by diagonalizing the nematic order parameter tensor

$$\mathcal{Q}_{\alpha\beta} = \frac{1}{N} \sum_{i=1}^N \left[ \frac{3}{2} \mathbf{u}_{i\alpha} \mathbf{u}_{i\beta} - \frac{1}{2} \delta_{\alpha\beta} \right],$$

where  $\mathbf{u}_{i\alpha}$  is the  $\alpha$ -component of the unit vector describing the orientation of the long axis of the rod  $i$ ,  $N$  is the number of rods in the slab, and  $\delta_{\alpha\beta}$  the Kronecker delta. The global nematic order parameter  $S$  is defined as the largest eigenvalue of  $\mathcal{Q}$  and the corresponding eigenvector is the nematic director  $\mathbf{n}$ .  $S$  ranges from  $-0.5$  to  $1$ . In addition, we define as introduced in<sup>1</sup> the local nematic order parameter  $S_i$  of particle  $i$  as

$$S_i = \frac{1}{n_i} \sum_{j=1}^{n_i} \left[ \frac{3}{2} (\mathbf{u}_i \cdot \mathbf{u}_j)^2 - \frac{1}{2} \right],$$

with  $n_i$  the number of neighbors of particle  $i$  and where two particles are considered neighbors if  $\rho_{ij} < 1.0 D$ , with  $\rho_{ij}$  the minimum surface-to-surface distance. We take  $D = D_{eff}$  in case of the experiments, whereas  $D$  equals the hard-core diameter of the spherocylinders in case of the simulations.  $S_i$  also ranges from  $-0.5$  (particle transverse to its neighbors) to  $1$  (perfect alignment).

The global smectic order can be probed by calculating the following order parameter<sup>2-5</sup>:

$$\tau = \max_l \left| \sum_{j=1}^N e^{2\pi i \mathbf{r}_j \cdot \mathbf{n} / l} \right|,$$

where the value of  $l$  that maximizes the above expression is identified as the layer spacing  $d$ . However, due to the limited statistics (small number of layers within confocal snapshot) and fluctuations in their positions, we obtained values of  $\tau$ , smaller than what one would expect after visual inspection of the sample, and a rather noisy trend of  $\tau$  as a function of height.

We therefore introduce a novel order parameter to quantify the local tendency of the particles to form (single) smectic or crystalline layers and we use it as a local smectic order parameter.

<sup>a</sup> Soft Condensed Matter, Debye Institute for Nanomaterials Science, Utrecht University, Princetonplein 5, 3584 CC Utrecht, The Netherlands

<sup>b</sup> Present address: State Key Laboratory of Polymer Physics and Chemistry, Institute of Chemistry, Chinese Academy of Sciences, No.2 1st North Street Zhongguancun, Beijing, 100190, China

\* Corresponding Author: henriette.bakker@gmail.com

\*\* Corresponding Author: a.vanblaaderen@uu.nl

We first calculate the shift  $h_{ij}$  of the center of mass of particle  $i$  with respect to its neighbors  $j$  projected on a common axis (we pick the main orientation  $\mathbf{u}_i$  of particle  $i$  but another direction such as the local nematic director would give similar results). We then normalize it and define:

$$\Delta_i = 1 - \frac{1}{m_i} \sum_{j=1}^{m_i} \frac{h_{ij}}{r_{cut}} = 1 - \left( \frac{1}{m_i} \sum_{j=1}^{m_i} \frac{\mathbf{r}_{ij}}{r_{cut}} \cdot \mathbf{u}_i \right),$$

where  $r_{cut} = (L_i + D)/2$  and  $m_i$  is the number of neighbors of particle  $i$  satisfying  $r_{ij} < r_{cut}$ , with  $r_{ij}$  the center-to-center distance between the rods.  $\Delta_i = 1$  corresponds to the orthogonality condition between  $r_{ij}$  and the common axis (in this case  $\mathbf{u}_i$ ). However, such a condition can be obtained both for perfectly aligned rods and in the case of transverse order (Supplementary Fig. S8). Notice that transverse rods are anyway expected in the smectic phase due to thermal fluctuations but we want to consider them as defects in a perfectly layered structure. In order to discriminate between these two configurations  $\Delta_i$  is then multiplied by  $S_i$ . In conclusion, we define the local smectic order parameter as

$$\tau_i \equiv S_i \Delta_i$$

Using  $\tau_i$  we are able to distinguish (locally) the smectic order (high values of  $\tau_i$ ) from the isotropic, nematic, as well as columnar order for which we expect low values of  $\tau_i$ . Note that the neighbor definition in  $\Delta_i$  and  $\tau_i$  is different and that the precise threshold value of the cut-off distance yields some degree of arbitrariness in the use of these order parameters to define the different phases. Furthermore, other approaches to define a local smectic order parameter are in principle possible, for example by considering.

$$\max_l \left| \sum_{j=1}^{n_i} e^{2\pi i \mathbf{r}_{ij} \cdot \mathbf{u}_i / l} \right|,$$

with  $r_{ij}$  the center-to-center distance between particle  $i$  and its neighbors  $j$ , defined as particles that have a minimum surface-to-surface distance  $\rho_{ij} < 1.0D$  (as for  $S_i$ ). However, to avoid misidentifications a large number of neighbors  $n_i$  are needed, otherwise even particles in the isotropic phase could have a large value of such an order parameter. When imposing this kind of threshold on the number of neighbors, we found similar results as using  $\tau_i \equiv S_i \Delta_i$ .

We expect that future work on order parameters for anisotropic particles based on the local environment will refine the family of quantities needed to discriminate between the different liquid crystal phases, in analogy with what happened to the bond orientational order parameter for crystal symmetries of spherical particles<sup>6,7</sup>. Such order parameters will be central in experimental studies on e.g. nucleation, glass transition and defects re-arrangement. Nevertheless, the order parameter  $\tau_i \equiv S_i \Delta_i$  introduced here is suitable for the current purpose, i.e., the identification of the smectic order in absence of a large number of smectic layers.

### SI 3 Determining different phases in the bulk phase diagram from experimental data

In order to distinguish between the different phases in experimental data, we rely on the local order parameters  $S_i$  and  $\tau_i$  for each particle  $i$ , as described above. Notice that the analysis of the local order parameters was based on the lengths  $L_i$  of the rods obtained by the particle tracking procedure, where the end-to-end length is defined as  $L = L_i + D$ , therefore are based on fluorescent shells present inside the rods. Subsequently, we determine the averaged values  $\langle S_i \rangle$  and  $\langle \tau_i \rangle$  by averaging over all particles in a certain slab in the sediment. The choice of the threshold values of the local order parameters at which we define the transition is admittedly somewhat arbitrary and can influence the identification of the different phases. Therefore, we chose values close to points of inflection observed in the trend of the averaged local order parameters (see Supplementary Fig. S9). We used the following threshold values to determine in the experimental system the different phases; isotropic (I) if  $\langle S_i \rangle < 0.5$  and  $\langle \tau_i \rangle < 0.35$ , nematic (N) if  $\langle S_i \rangle > 0.5$  and  $\langle \tau_i \rangle < 0.35$ , Sm<sub>2</sub> if  $\langle S_i \rangle > 0.5$  and  $\langle \tau_i \rangle > 0.35$ . Analysis based on global order parameters is also in principle possible but usually more noisy due to the need to collect a larger amount of data. In particular the traditional global smectic order parameter,  $\tau$  is sensitive to fluctuations of the layers and defects in and between layers.

## SI 4 Estimating the bulk phase diagram from computer simulations

The colloidal silica spheres and rods are modeled as hard spheres of diameter  $\sigma$  and hard spherocylinders of (cylinder) length  $L_{cyl}$  and diameter  $D$ , respectively. Where the experimental end-to-end length  $L$  is defined as  $L = L_{cyl} + D$ . Particles interact via a purely excluded-volume pair potential:  $U = \infty$  if two particles overlap,  $U = 0$  otherwise. We first perform Monte Carlo (MC) simulations in the  $NPT$  ensemble of 1600 hard spherocylinders to map the behaviour of the experimental (single-component) system of silica rods onto hard particle behaviour, i.e., identify the effective dimensions of the silica rods (see Supplementary Fig. S7 and discussion above). After this analysis, we simulate  $N_{tot} = N_{sph} + N_{rods} = 3125$  hard spheres and hard spherocylinders ( $L_{cyl} = 6.46\sigma$ ,  $D = 1.52\sigma$ ,  $L_{cyl}/D \sim 4.25$ ) in the  $NPT$  ensemble with various composition  $x_{sph} = N_{sph}/N_{tot}$ . Each simulation consists of several million of MC steps, where one step is defined as  $N_{tot}$  moves randomly chosen from sphere translation, rod translation, rod rotation, and either isotropic or anisotropic change of the simulation box volume. Initial configurations at a given composition  $x$  are obtained from an equilibrated configuration at lower  $x$  by replacing an appropriate number of rods with spheres. Each state point has been characterized by several order parameters, some of which have been introduced before and used for the experimental data as well.

According to theoretical predictions based on a second-virial density functional theory applied to a rod-sphere mixture with similar sizes ( $L_{cyl}/\sigma = 7$ ,  $D = \sigma$ ), we expect stable isotropic (I), nematic (N) and binary-smectic ( $Sm_2$ ) liquid crystal phases<sup>8</sup>. In our study, we do not take into account the possible crystalline (hexagonal) order, neither within a single layer nor between different layers, and therefore we do not distinguish between (binary) Smectic-A and (binary) Smectic-B and possible (binary) crystal phases, even though we observe hexagonal arrangements of rods, both in experiments and in simulations. Since for the short rods considered here both the I-N and the N- $Sm_2$  transitions are weakly first order<sup>9</sup>, and a particularly broad I- $Sm_2$  coexistence region is expected when such rods are mixed with hard spheres<sup>8</sup>, an accurate identification of the phase boundaries is clearly challenging. Nevertheless, we use both global and local order parameters to discriminate between the different liquid crystalline structures for a large number of state points (for which  $x_{sph}$  and  $P$  are imposed) and trace the state diagram of rod-sphere mixtures for which experiments have been performed (see Supplementary Fig. S10a). In particular, in the isotropic phase (see Supplementary Fig. S10b) all the order parameters vanish. The nematic phase (see Supplementary Fig. S10c) is characterized by a high value of the nematic order parameter (both the global  $S$  and the local  $S_i$  as can be seen from the color coding of the rods) but not of the smectic ones, since neither the rods nor the spheres form layers. We observe that the I-N shifts towards higher pressure upon increasing composition  $x_{sph}$  until a point (around  $x_{sph} \simeq 0.6$ ) beyond which the nematic phase is no longer stable. In the  $Sm_2$  phase (see Supplementary Fig. S10d) the rods locally form layers resulting in a large value of the local

smectic order parameter  $\tau_i$  as shown by the color coding. The structure is clearly long-range which is also confirmed by the (ordinary) global smectic order parameter  $\tau$ . The binary character of the smectic phase is confirmed by the fact that the spheres are also arranged in layers, as clearly evident from the snapshot in Supplementary Fig. S10(d). Such layering can also be quantified by a global smectic order parameter for the spheres, calculated along the nematic director of the rods  $\mathbf{n}$  (that coincides with the layer normal), in full analogy with the one for the rods (see section on order parameters):

$$\tau_{sph} = \max_l \left| \sum_{j=1}^N e^{2\pi i \mathbf{r}_j \cdot \mathbf{n}/l} \right|.$$

Both the values of  $\tau_{sph}$  and the associated spacing between layers of spheres are consistent with the values of  $\tau$  (for only rods) and the spacing between the smectic layers of the rods, as expected for the  $Sm_2$  phase. However, for small compositions  $x_{sph}$  and large pressures  $P$  (see Supplementary Fig. S10e-f), the spheres do not form layers anymore but rather are expelled from the layers of rods and organize themselves into linear aggregates. This structure is likely not a novel thermodynamically stable phase but rather should be considered as an indication of the underlying phase separation into a sphere-rich isotropic phase and rod-rich (binary) smectic phase (or probably a crystal phase of rods at sufficiently high pressures, as evident from Supplementary Fig. S10e). Indeed, since the system cannot really demix because of the finite size nature of the simulations, the spheres have to act as substitutes of rods to minimize the overall system free volume. It is important to remark that this columnar arrangement of spheres is not related to the columnar phase observed in the mixture of colloidal spheres and *fd*-viruses<sup>10</sup>, since in that case the columns of spheres are perpendicular to the direction of the layers of the rods. The possibility of forming that structure with only hard-core interactions and its thermodynamic stability are still open questions.

The transition from a stable  $Sm_2$  phase to this kinetically trapped structure, that is evidence of I- $Sm_2$  demixing, is often associated with a drop in  $\tau_{sph}$  as reported in the Supplementary Fig. S11f. As can be seen from the Supplementary Fig. S10f, the formation of columns of spheres occurs also when most of the spheres are still arranged in layers, therefore yielding to a somehow arbitrary definition of the upper bound of the  $Sm_2$  stability region.

For larger values of  $x_{sph}$ , the I- $Sm_2$  demixing is more evident as can be appreciated from Supplementary Fig. S10g-h in which a number of smectic layers (depending on  $x_{sph}$ ) is in coexistence with an isotropic phase rich in spheres. This behaviour is also captured by the probability distribution of rods having a certain value of the local smectic order parameter  $\tau_i$  (some examples are reported in the Supplementary Fig. S11a). Indeed, for state points inside the I- $Sm_2$  regions two populations of particles (one with  $|\tau_i| \sim 0$  and one with  $\tau_i$  bigger than a given threshold) are often evident. However, extracting the equilibrium composition of the two coexisting phases based on the amount of particles in the two populations seemed to be not an easy task due to the limited system size of our simulations and the sensitivity on the

choice of the threshold value. By examining the state diagram obtained, we notice that compositions around  $x_{sph} = 0.6$  show a peculiar *re-entrant* sequence upon increasing the pressure, going from an isotropic to I-Sm<sub>2</sub> region to a pure Sm<sub>2</sub> to a demixed region again. Representative snapshots at this composition, along with a quantitative analysis, are reported in the Supplementary Fig. S11. Finally, we notice that the topology of the phase diagram here reported is consistent with theoretical predictions<sup>8</sup>, including the re-entrant behaviour of the Sm<sub>2</sub> region.

We wish to remark here that simulations in the  $NPT$  ensemble, in which the overall composition  $x_{sph}$  and pressure  $P$  are kept fixed, is not always the most convenient statistical ensemble to study broad demixing transitions as huge system sizes and long simulation times are need to obtain phase coexistence between different thermodynamic states. Indeed, a standard procedure to trace the phase diagram of a mixture would require simulations in the grand-canonical ensemble that are, however, not feasible for short rods (only the insertion/removal of the small spheres would be possible). Recently, the use of hard walls in computer simulations of rod-sphere systems composed of similar number of particles as used here and similar particle dimensions, have been employed as an alternative to determine slightly more accurately the variation in composition of the isotropic-nematic transition but limiting the study to a small region in the  $x_{sph} - P$  plane<sup>11</sup>. However, at the densities where the binary smectic phase is observed, the effect of walls would be still quite pronounced for ordinary system sizes. Ultimately, an accurate study of the equilibrium phase behaviour should be based on (computationally expensive) free-energy calculations, but this is beyond the scope of the present work.

## SI 5 Supplemental Figures

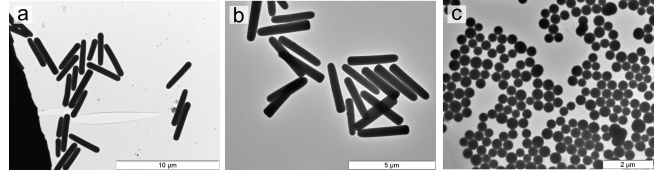


Fig. S1 TEM images of particles used. (a) R2 rods, with  $L = 3.6 \mu\text{m}$  ( $\delta_L \simeq 18\%$ ),  $D = 0.59 \mu\text{m}$  ( $\delta_D \simeq 10\%$ ),  $L/D = 6.1$ . (b) R1 rods, with  $L = 2.9 \mu\text{m}$  ( $\delta_L \simeq 9\%$ ),  $D = 0.51 \mu\text{m}$  ( $\delta_D \simeq 9\%$ ),  $L/D = 5.6$ . (c) Spheres, with  $\sigma = 385 \text{ nm}$  ( $\delta_\sigma \simeq 9\%$ )

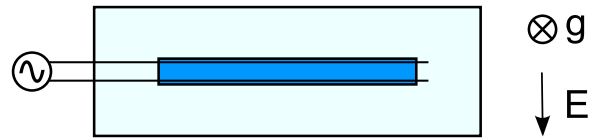


Fig. S2 Schematic representation of the electric sample cell. Schematic representation of the used sample cell for the alignment with an ac-electric field, field perpendicular to gravity.

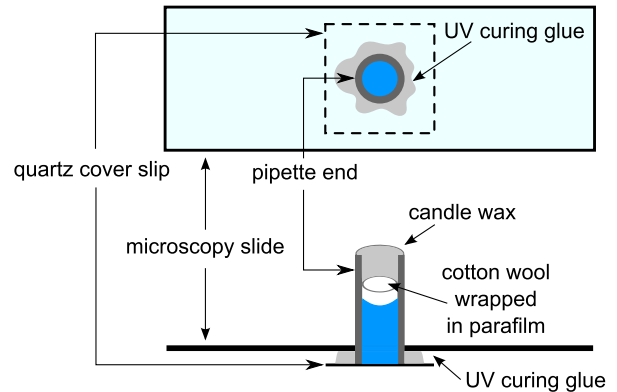


Fig. S3 Schematic representation of sample cell. Schematic representation of the used sample cell to study the sedimentation profile of mixtures of colloidal rods and spheres with 3D confocal microscopy.

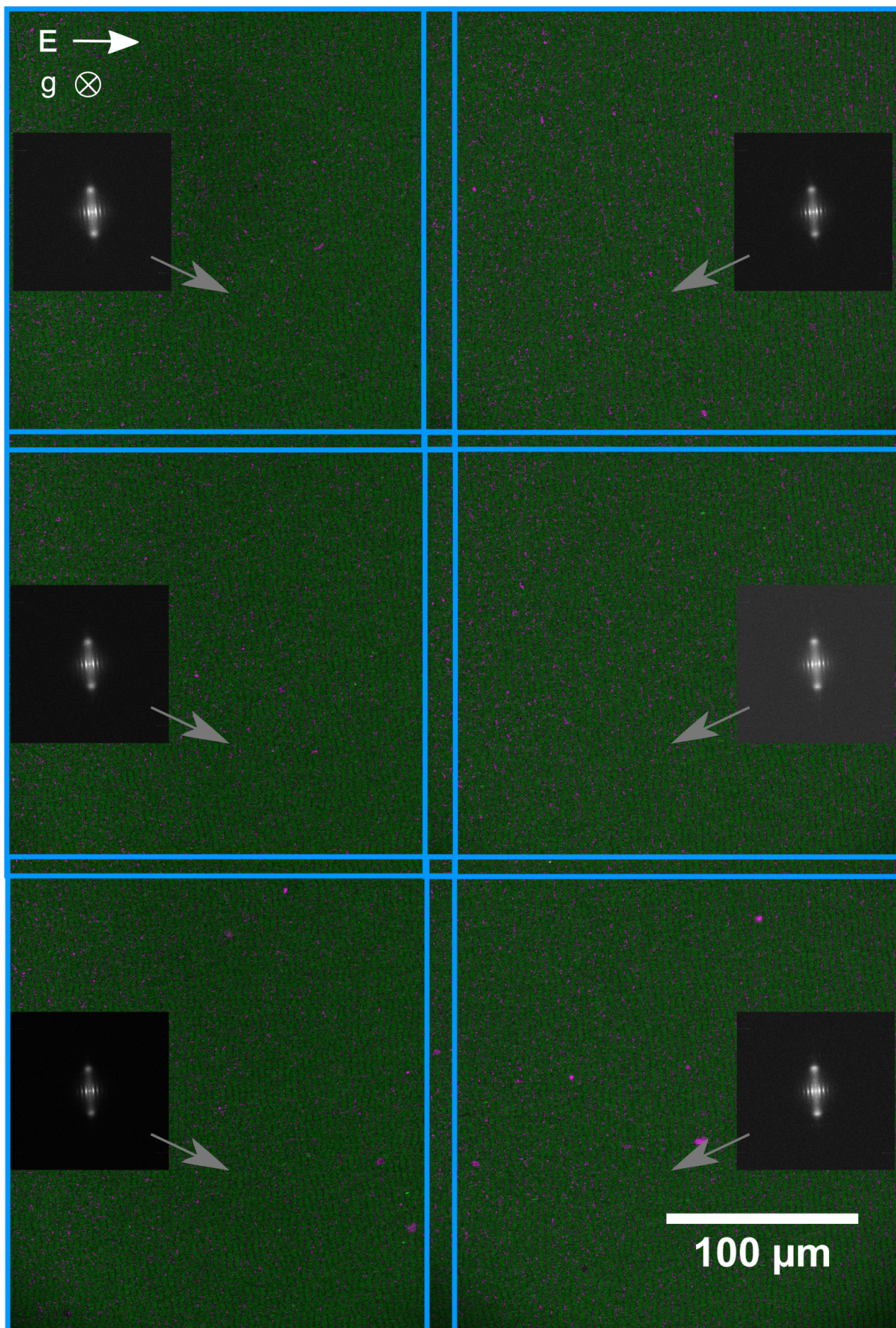


Fig. S4 Confocal image of an aligned  $\text{Sm}_2$ -phase using an AC-electric field. Confocal image ( $738 \mu\text{m} \times 492 \mu\text{m}$ ) of obtained  $\text{Sm}_2$ -phase with an ac-electric field switched on during sedimentation ( $15 \text{ V mm}^{-1}$ ). The image consists of 6 images stitched together to form 1 image.

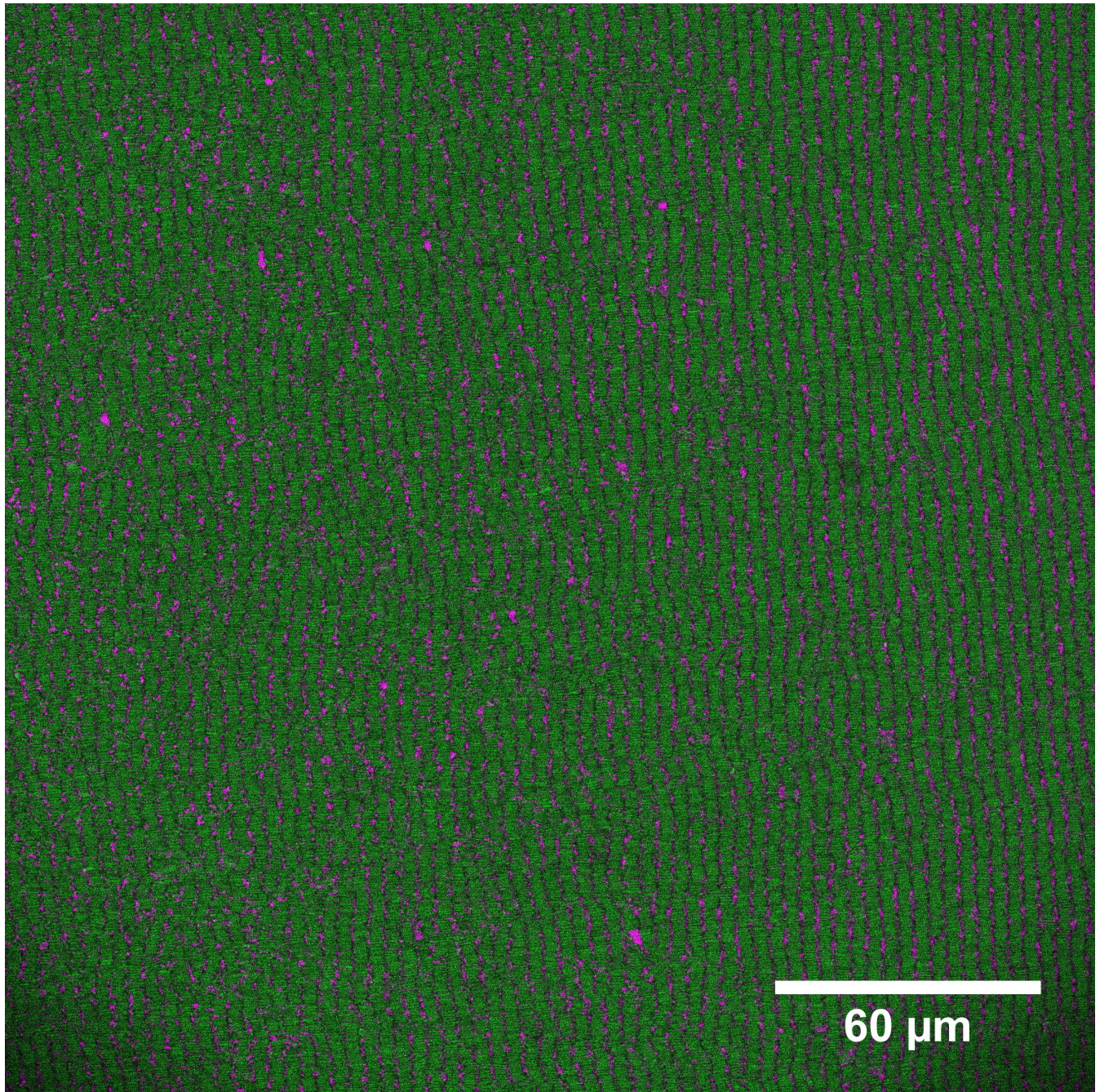


Fig. S5 Confocal image of an aligned  $\text{Sm}_2$ -phase using an AC-electric field. Top right confocal image ( $246 \mu\text{m} \times 246 \mu\text{m}$ ) in Supplementary Fig. S4.

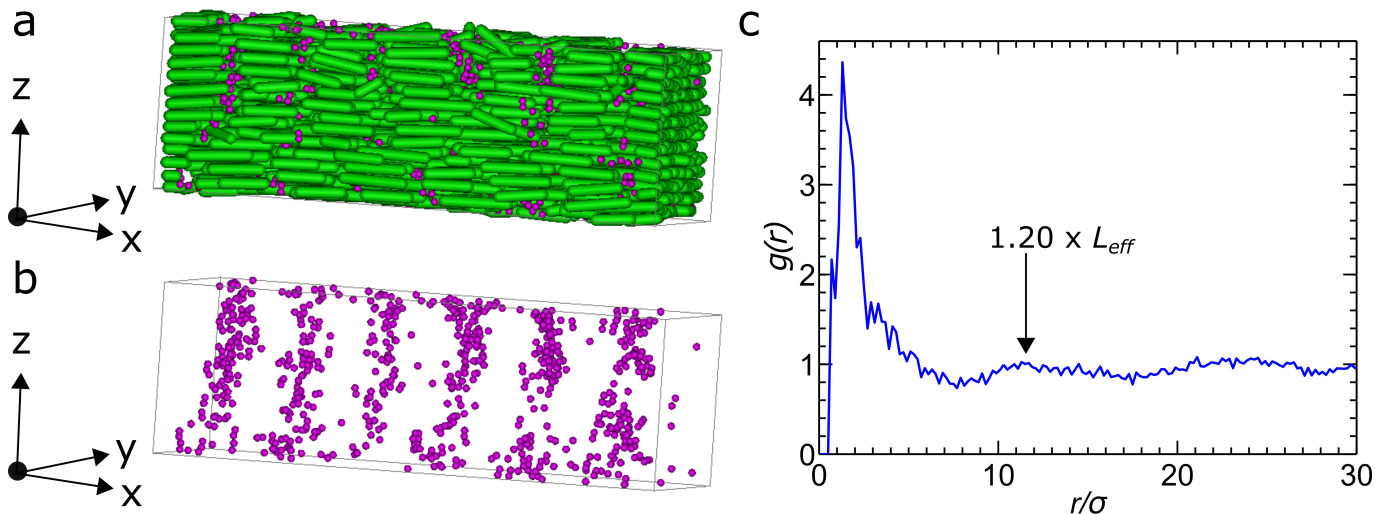


Fig. S6  $g(r)$  of spheres inside  $Sm_2$ -phase. (a-b) Computer drawn images from fitted particles of part of a confocal data stack of a sediment of rods and spheres, showing the  $Sm_2$ -phase (a) depicted both rods and spheres (b) depicted only spheres. (c)  $g(r)$  of spheres inside the  $Sm_2$ -phase, data taken from (b). We observe a peak at  $11.6\sigma$ , with  $\sigma$  being the bare diameter of the spheres. This corresponds to a smectic layer spacing of  $1.20L_{eff}$ , with  $L_{eff}$  being the average effective length of the rods. From simulation<sup>12</sup> of only rods with  $L_{cyl}/D = 5$  ( $L/D = 6$ ) a spacing of 1.048 is expected. Kuijk *et al* experimentally found a spacing between 1.1 and 1.2  $L_{eff}$  for silica rods<sup>13</sup>. The effective sphere diameter  $\sigma_{eff}$  is  $0.13L_{eff}$ .

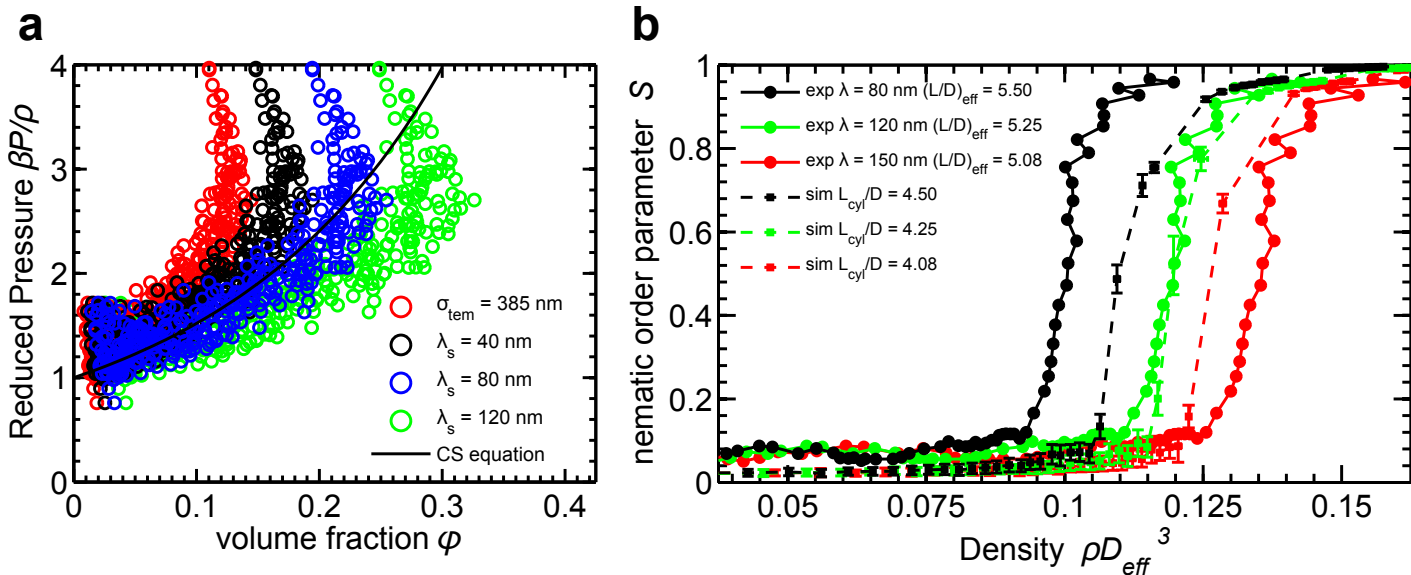


Fig. S7 Determination of the effective particle dimensions. (a) Fit to the Carnahan-Starling equation of state. The pressure (open symbols), as obtained by integrating the density profile of the spheres for the top part of a sediment of rods and spheres, was mapped to the CS equation of state (solid line), in order to obtain the effective diameter of the particles. Spheres with  $\sigma_{eff} = \sigma_{tem} + \lambda_s$  and  $\lambda_s = 80$  nm could be mapped as hard particles to the CS equation of state. This resulted in an effective diameter of the spheres:  $\sigma_{eff} = 465$  nm. (b) Plot of the global nematic order parameter  $S$  as a function of density, at the I-N transition. Experimental data points are shown as the solid lines with circles. Simulations are shown as dashed lines and squares. Experimental data with rods  $D_{eff} = D_{tem} + \lambda_r$ , with  $\lambda = 120$  nm match best with data from simulations. This resulted in the following effective dimensions for the R2 rods:  $D_{eff} = 707$  nm,  $L_{eff} = 3711$  nm,  $(L/D)_{eff} = 5.25$ ,  $D_{eff} = 1.52\sigma_{eff}$ .

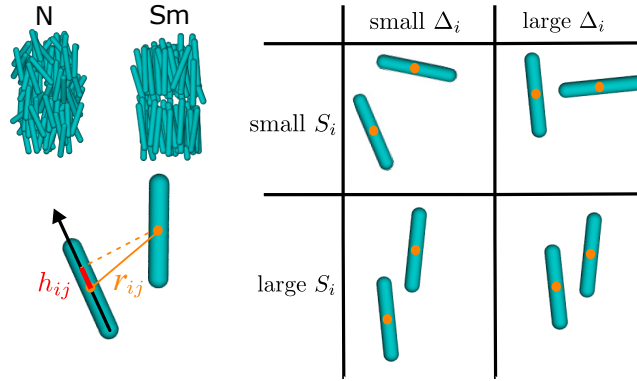


Fig. S8 Schematic of the smectic local order parameter. Schematic of the smectic local order parameter  $\tau_i = S_i \cdot \Delta_i$

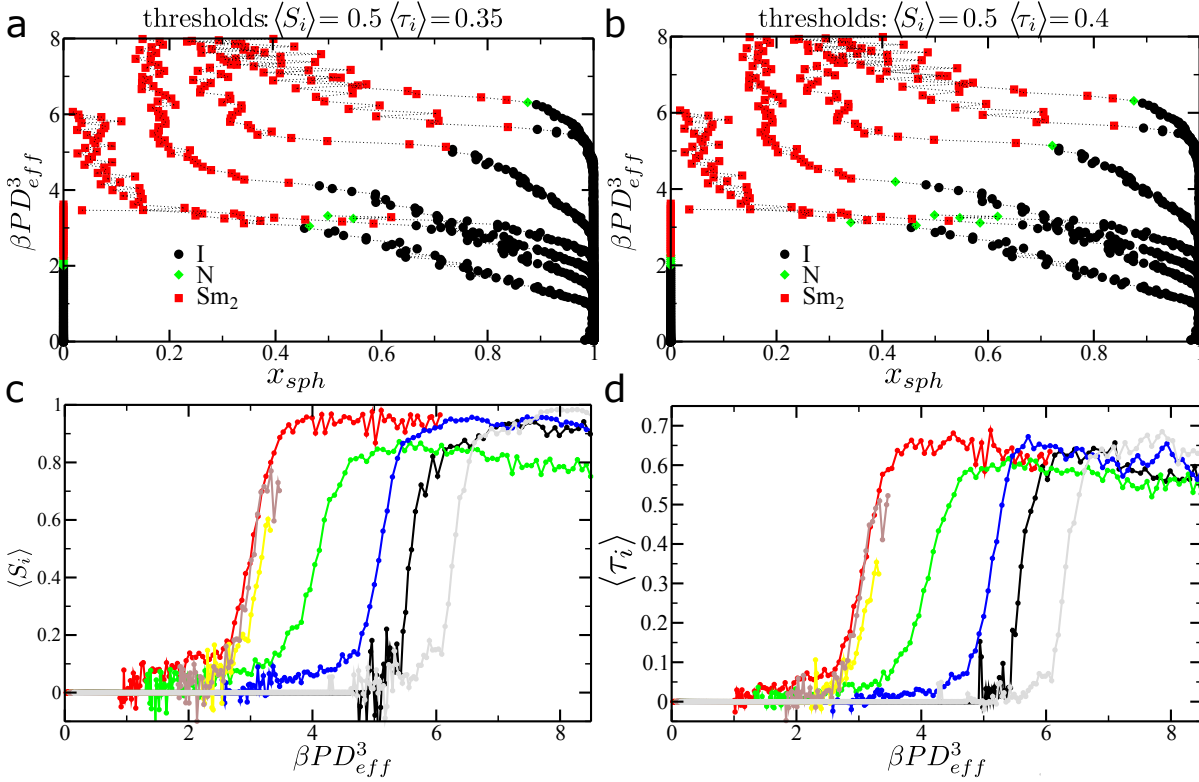


Fig. S9 Experimental State Diagram and Order Parameters. (a) Experimental state diagram (as Fig. 4 of the main text), using the following thresholds: isotropic (I) if  $\langle S_i \rangle < 0.5$  and  $\langle \tau_i \rangle < 0.35$  (black circles), nematic (N) if  $\langle S_i \rangle > 0.5$  and  $\langle \tau_i \rangle < 0.35$  (green diamonds), Sm<sub>2</sub> if  $\langle S_i \rangle > 0.5$  and  $\langle \tau_i \rangle > 0.35$  (red squares). (b) Different choice of the threshold values for the local smectic order parameter  $\tau_i$ , isotropic (I) if  $\langle S_i \rangle < 0.5$  and  $\langle \tau_i \rangle < 0.4$ , nematic (N) if  $\langle S_i \rangle > 0.5$  and  $\tau_i < 0.4$ , Sm<sub>2</sub> if  $\langle S_i \rangle > 0.5$  and  $\langle \tau_i \rangle > 0.4$ . (c) Averaged local nematic order parameter  $\langle S_i \rangle$  as a function of reduced pressure  $\beta PD_{eff}^3$  for different equilibrated sediments. (d) Averaged local smectic order parameter  $\langle \tau_i \rangle$  for different equilibrated sediments.

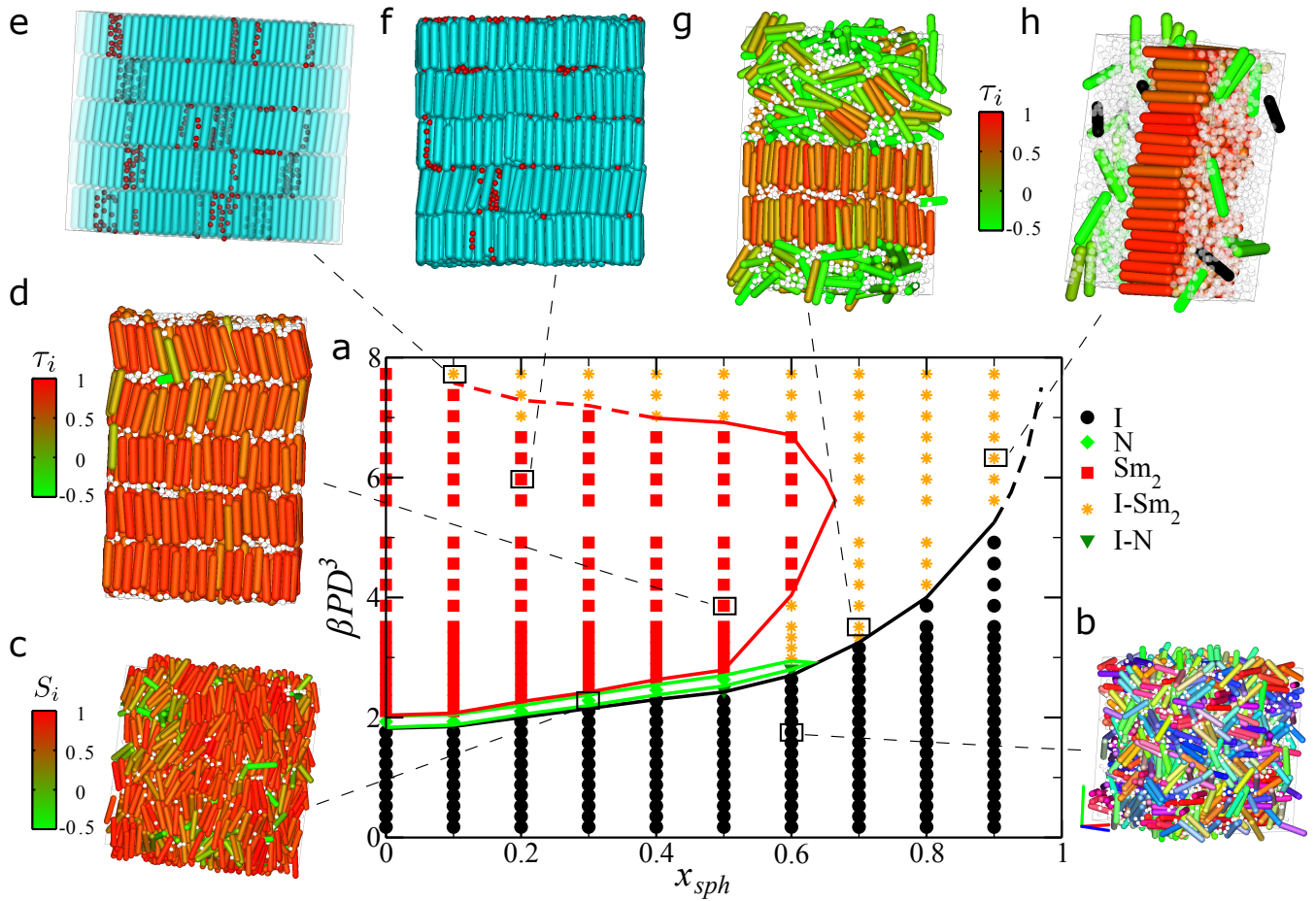


Fig. S10 State diagram from bulk MC-NPT simulations. (a) State diagram from bulk MC-NPT simulations. Representative snapshots for (b) isotropic phase (I) with  $x_{sph} = 0.6 \beta PD^3 = 1.93$ , rods are colored according to their orientation (axis colors indicated in the snapshot); (c) nematic phase (N)  $x_{sph} = 0.3 \beta PD^3 = 2.28$  with rods colored according to the local nematic order parameter  $S_i$ ; (d) binary smectic phase ( $Sm_2$ )  $x_{sph} = 0.5 \beta PD^3 = 3.86$  with rods colored according to the local smectic order parameter  $\tau_i$ ; (e) Formation of columnar aggregates of hard spheres as indication of demixing between a smectic (or crystal) phase rich in rods and an isotropic phase rich in spheres.  $x_{sph} = 0.1 \beta PD^3 = 7.73$ ; (f) Columns of spheres start to appear in a  $Sm_2$  phases (most of the spheres are still arranged in layers)  $x_{sph} = 0.2 \beta PD^3 = 5.97$ ; (g) Coexistence between I and  $Sm_2$  phase,  $x_{sph} = 0.7 \beta PD^3 = 3.86$ , rods colored according to  $\tau_i$ ; (h) Single layer of rods in coexistence with a sphere-rich isotropic phase,  $x_{sph} = 0.9 \beta PD^3 = 6.32$ , rods are colored according to  $\tau_i$ .

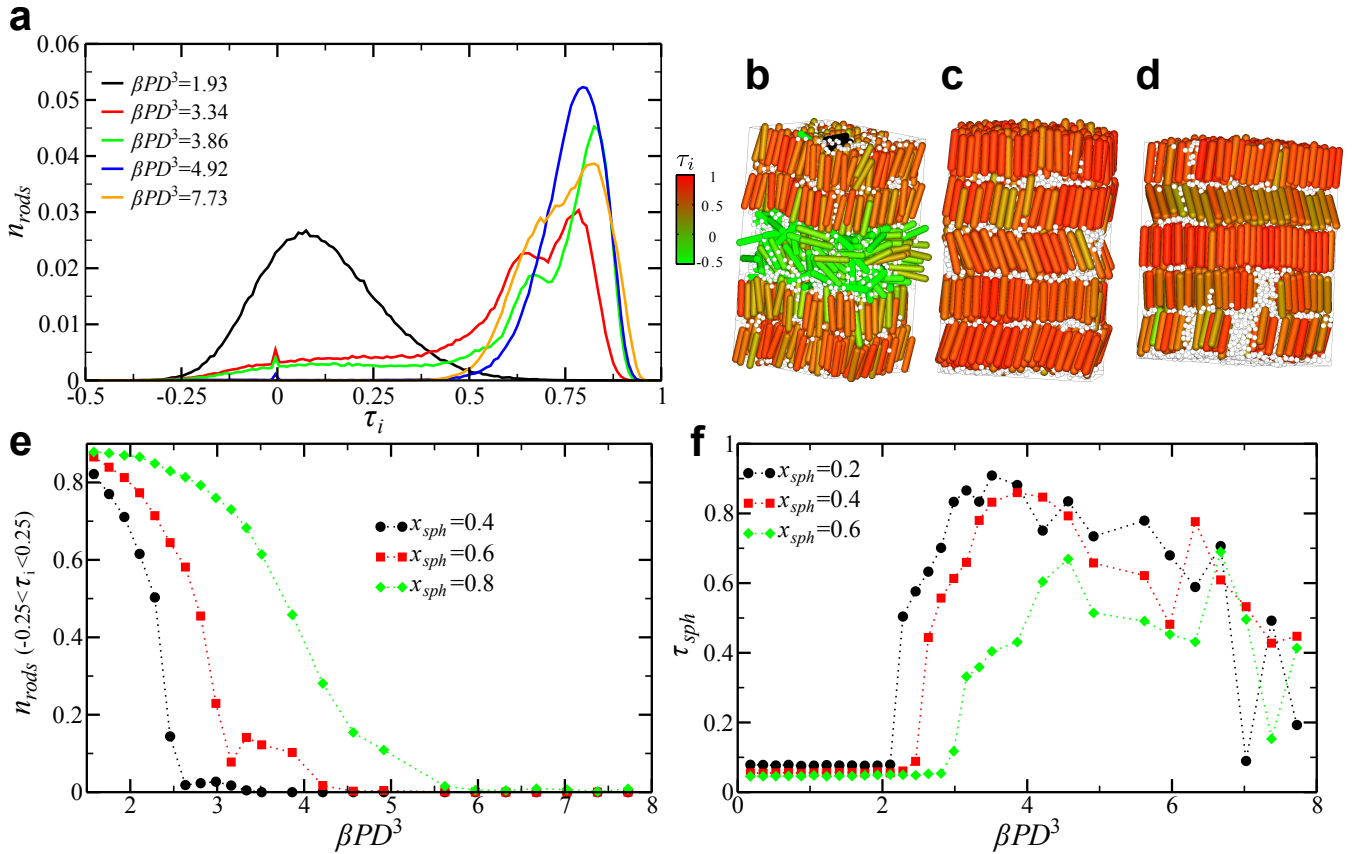


Fig. S11 Identifying coexistence between isotropic and binary smectic phase. (a) Fraction of rods  $n_{rods}$  with a given value of the local smectic order parameter  $\tau_i$  for state points with  $x_{sph} = 0.6$  and reduced pressures  $\beta PD^3$  as indicated in the legend.  $\beta PD^3 = 1.93$  corresponds to an isotropic state (representative snapshot in Supplementary Fig. S10(b)).  $\beta PD^3 = 3.34$  corresponds to a two-phase I-Sm<sub>2</sub> coexistence state (typical snapshot in panel (b)), a small peak at  $\tau_i \sim 0$  is evident.  $\beta PD^3 = 4.92$  corresponds to a Sm<sub>2</sub> state (snapshot in panel (c)).  $\beta PD^3 = 7.73$  corresponds to a I-Sm<sub>2</sub> state (snapshot in panel (d)). In this case the probability distribution of  $\tau_i$  is not useful to identify the state point but the low value of  $\tau_{sph}$  (see panel (f)) indicates that the spheres are not arranged in layers. In all the snapshots the rods are colored from green (low) to red (high) according to the value of  $\tau_i$ . Rods that are colored black do not have neighbors and therefore have  $\tau_i = 0$ . Peaks around zero (panel (a)) are evidences of demixing between I and Sm<sub>2</sub>. Tracking the number of rods with small values of  $\tau_i$  could help in identifying the state point. In panel (e) the fraction of rods  $n_{rods}$  with a small  $\tau_i$  (arbitrarily chosen such that  $|\tau_i| < 0.25$ ) are plotted as a function of the reduced pressure  $\beta PD^3$  for different composition  $x_{sph}$ . For  $x_{sph} = 0.6$  the non-monotonic behaviour of  $n_{rods}$  could be used to identify the re-entrant behaviour of the Sm<sub>2</sub> region, even if it is admittedly somehow arbitrary. In panel (f) the smectic order parameter associated to layers of spheres  $\tau_{sph}$  (see text for the definition) is plotted against the pressure for different composition. The different arrangement of spheres, either in layers or in columns/random aggregates (these are indications of I-Sm<sub>2</sub> demixing) is associated to a large or small value of  $\tau_{sph}$ , respectively.

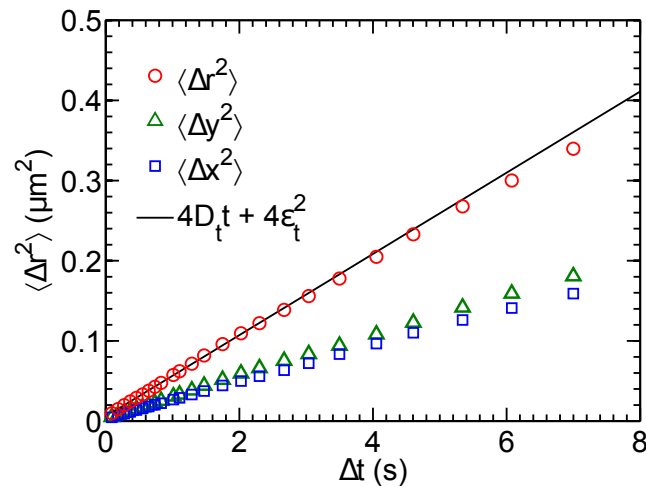


Fig. S12 Experimental measurements of the mean square displacement on a dilute suspension of 385 nm RITC-labeled silica spheres,  $D_t = 1.3 \times 10^{-2} \mu\text{m}^2 \text{s}^{-1}$  and  $\varepsilon_t = 38 \text{ nm}$ .

Table S1 Properties of particles used in this paper. Here,  $L$  is the end-to-end length of the rods,  $D$  is the diameter of the particles,  $\delta$  is the polydispersity of the particles and  $l_g$  is the gravitational length of the particle based upon a 85 wt% glycerol-water mixture and the particle dimensions measured by TEM. The aspect ratio for simulations is defined as  $L_{cyl}/D = (L/D)_{eff} - 1$ .

	Particle dimensions from TEM					Effective particle dimensions			
	$L$ nm	$\delta_L$ %	$D$ nm	$\delta_D$ %	$L/D$	$l_g$ $\mu\text{m}$	$L_{eff}$ nm	$D_{eff}$ nm	$(L/D)_{eff}$
<b>R2</b>	3591	18	587	10	6.1	0.64	3711	707	5.25
<b>R1</b>	2860	9	510	9	5.6	1.06	2980	630	4.75
<b>Spheres</b>			385	9		17.65		465	

## References

- 1 A. Cuetos, B. Martínez-Haya, S. Lago and L. F. Rull, *Phys. Rev. E*, 2007, **75**, 1–12.
- 2 P. de Gennes, *The Physics of Liquid Crystals.*, Clarendon Press, Oxford, 1974.
- 3 M. Cifelli, G. Cinacchi and L. De Gaetani, *J. Chem. Phys.*, 2006, **125**, 164912.
- 4 W. L. McMillan, *Phys. Rev. A.*, 1971, **4**, 1238–1246.
- 5 K. Kobayashi, *Phys. Lett. A*, 1970, **31**, 125–126.
- 6 P. J. Steinhardt, D. Nelson and M. Ronchetti, *Physical Review B*, 1983, **28**, 784–805.
- 7 W. Lechner and C. Dellago, *J. Chem. Phys.*, 2008, **129**, 114707.
- 8 G. Cinacchi, E. Velasco and L. Mederos, *J. Phys.: Condens. Matter*, 2004, **16**, S2003–S2014.
- 9 P. Bolhuis and D. Frenkel, *J. Chem. Phys.*, 1997, **106**, 666–687.
- 10 M. Adams, Z. Dogic, S. L. Keller and S. Fraden, *Nature*, 1998, **393**, 349–352.
- 11 L. Wu, A. Malijevský, G. Jackson, E. A. Müller and C. Avendaño, *J. Chem. Phys.*, 2015, **143**, 044906.
- 12 A. Patti, D. El Masri, R. van Roij and M. Dijkstra, *J. Chem. Phys.*, 2010, **132**, 224907.
- 13 A. Kuijk, D. V. Byelov, A. V. Petukhov, A. van Blaaderen and A. Imhof, *Farad. Discuss.*, 2012, **159**, 181–199.